

Efficient spectroscopy of single embedded emitters using optical fiber taper waveguides

Marcelo Davanço^{1,2} and Kartik Srinivasan¹

¹Center for Nanoscale Science and Technology, National Institute of Standards and Technology, Gaithersburg, MD, 20899-6203

²Maryland NanoCenter,
University of Maryland, College Park, MD, 20742

mdavanco@nist.gov

Abstract: A technique based on using optical fiber taper waveguides for probing single emitters embedded in thin dielectric membranes is assessed through numerical simulations. For an appropriate membrane geometry, photoluminescence collection efficiencies in excess of 10 % are predicted, exceeding the efficiency of standard free-space collection by an order of magnitude. Our results indicate that these fiber taper waveguides offer excellent prospects for performing efficient spectroscopy of single emitters embedded in thin films, such as a single self-assembled quantum dot in a semiconductor membrane.

© 2009 Optical Society of America

OCIS codes: (300.6280) Spectroscopy, fluorescence and luminescence; (350.4238) Nanophotonics and photonic crystals; (230.7370) Waveguides; (230.5590) Quantum-well, -wire and -dot devices; (180.4243) Near-field microscopy

References and links

1. B. Gerardot, S. Seidl, P. Dalgarno, R. Warburton, M. Kroner, K. Karrai, A. Badolato, and P. Petroff, "Contrast in transmission spectroscopy of a single quantum dot," *Appl. Phys. Lett.* **90**, 221 106 (2007).
2. A. N. Vamivakas, M. Atature, J. Dreiser, S. T. Yilmaz, A. Badolato, A. K. Swan, B. B. Goldberg, A. Imamoglu, and M. S. Unlu, "Strong Extinction of a Far-Field Laser Beam by a Single Quantum Dot," *Nano Lett.* **7**, 2892–2896 (2007).
3. G. Wrigge, I. Gerhardt, J. Hwang, G. Zumofen, and V. Sandoghdar, "Efficient coupling of photons to a single molecule and the observation of its resonance fluorescence," *Nat. Phys.* **4**, 60–66 (2008).
4. I. Gerhardt, G. Wrigge, P. Bushev, G. Zumofen, M. Agio, R. Pfab, and V. Sandoghdar, "Strong Extinction of a Laser Beam by a Single Molecule," *Phys. Rev. Lett.* **98**, 033 601 (2007).
5. T. Aoki, B. Dayan, E. Wilcut, W. P. Bowen, A. S. Parkins, H. J. Kimble, T. J. Kippenberg, and K. J. Vahala, "Observation of Strong Coupling between One Atom and a Monolithic Microresonator," *Nature* **443**, 671–674 (2006).
6. K. Srinivasan and O. Painter, "Linear and nonlinear optical spectroscopy of a strongly coupled microdisk-quantum dot system," *Nature* **450**, 862–865 (2007).
7. K. Srinivasan, C. P. Michael, R. Perahia, and O. Painter, "Investigations of a coherently driven semiconductor optical cavity QED system," *Phys. Rev. A* **78**, 033 839 (2008).
8. F. Le Kien, S. Dutta Gupta, V. I. Balykin, and K. Hakuta, "Spontaneous emission of a cesium atom near a nanofiber: Efficient coupling of light to guided modes," *Phys. Rev. A* **72**, 032 509 (2005).
9. V. V. Klimov and M. Ducloy, "Spontaneous emission rate of an excited atom placed near a nanofiber," *Phys. Rev. A* **69**, 013 812 (2004).
10. K. Nayak, P. Melentiev, M. Morinaga, F. Le Kien, V. Balykin, and K. Hakuta, "Optical nanofiber as an efficient tool for manipulating and probing atomic fluorescences," *Opt. Express* **15**, 5431–5438 (2007).
11. K. Srinivasan, O. Painter, A. Stintz, and S. Krishna, "Single quantum dot spectroscopy using a fiber taper waveguide near-field optic," *Appl. Phys. Lett.* **91**, 091 102 (2007).

12. A. Muller, E. B. Flagg, P. Bianucci, X. Wang, D. G. Deppe, W. Ma, J. Zhang, G. J. Salamo, M. Xiao, and C. K. Shih, "Resonance Fluorescence from a Coherently Driven Semiconductor Quantum Dot in a Cavity," *Phys. Rev. Lett.* **99**, 187 402 (2007).
13. A. W. Snyder and J. D. Love, *Optical Waveguide Theory* (Chapman and Hall, New York, 1983).
14. C. F. Wang, A. Badolato, I. Wilson-Rae, P. M. Petroff, E. Hu, J. Urayama, and A. Imamoglu, "Optical properties of single InAs quantum dots in close proximity to surfaces," *Appl. Phys. Lett.* **85**, 3423–3425 (2004).
15. W.-P. Huang, "Coupled-mode theory for optical waveguides: and overview," *J. Opt. Soc. Am. A* **11**, 963–983 (1994).
16. Lumerical FDTD Solutions. Specific software packages are identified in this paper to foster understanding. Such identification does not imply recommendation or endorsement by NIST, nor does it imply that the software identified is necessarily the best available for the purpose.
17. J. D. Jackson, *Classical Electrodynamics* (Wiley, New York, 1999), 3rd edn.
18. H. Benisty, R. Stanley, and M. Mayer, "Method of source terms for dipole emission modification in modes of arbitrary planar structures," *J. Opt. Soc. Am. A* **15**, 1192–1201 (1998).
19. H. Rigneault and S. Monneret, "Modal analysis of spontaneous emission in a planar microcavity," *Phys. Rev. A* **54**, 2356–2368 (1996).
20. H. P. Urbach and G. L. J. A. Rikken, "Spontaneous emission from a dielectric slab," *Phys. Rev. A* **57**, 3913–3930 (1998).
21. C. P. Michael, M. Borselli, T. J. Johnson, and O. Painter, "An optical fiber taper probe for wafer-scale microphotonic device characterization," *Opt. Express* **15**, 4745–4752 (2007).
22. P. Jayavel, H. Tanaka, T. Kita, O. Wada, H. Ebe, M. Sugawara, J. Tatebayashi, Y. Arakawa, Y. Nakat, and T. Akiyama, "Control of optical polarization anisotropy in edge emitting luminescence of InAs/GaAs self-assemble quantum dots," *Appl. Phys. Lett.* **84** (2004).
23. T. S ndergaard and B. Tromborg, "General theory for spontaneous emission in active dielectric microstructures: Example of a fiber amplifier," *Phys. Rev. A* **64**, 033 812 (2001).
24. Y. Xu, J. S. Vučković, R. K. Lee, O. J. Painter, A. Scherer, and A. Yariv, "Finite-difference time-domain calculation of spontaneous emission lifetime in a microcavity," *J. Opt. Soc. Am. B* **16**, 465–474 (1999).
25. Comsol Multiphysics. Specific software packages are identified in this paper to foster understanding. Such identification does not imply recommendation or endorsement by NIST, nor does it imply that the software identified is necessarily the best available for the purpose.
26. V. R. Almeida, Q. Xu, C. A. Barrios, and M. Lipson, "Guiding and confining light in void nanostructure," *Opt. Lett.* **29**, 1209–1211 (2004).
27. M. Davanço and K. Srinivasan, "Optical fiber taper waveguides for highly efficient spectroscopy of single emitters deposited on a dielectric slab," Manuscript in preparation (2009).
28. S. Koseki, B. Zhang, K. D. Greve, and Y. Yamamoto, "Monolithic integration of quantum dot containing microdisk microcavities coupled to air-suspended waveguides," *Appl. Phys. Lett.* **94**, 051 110 (2009).
29. M. Davanço and K. Srinivasan, "Fiber-coupled semiconductor waveguides as an efficient optical interface to a single quantum dipole," preprint: arxiv.org/abs/0905.2994 (2009).
30. C. W. Gardiner and M. J. Collett, "Input and output in damped quantum systems: Quantum stochastic differential equations and the master equation," *Phys. Rev. A* **31**, 3761–3774 (1985).
31. C. Cohen-Tannoudji, J. Dupont-Roc, and G. Grynberg, *Atom-Photon Interactions: Basic Processes and Applications* (Wiley Interscience, New York, 1998).

1. Introduction

The development of novel techniques for efficient detection and spectroscopy of individual quantum emitters in the solid state is essential for an understanding of the emitter and its relationship with the surrounding environment. Challenges involved with spectroscopy of such systems include tight focusing requirements and separation of the signal of interest from background scattered light due to the host crystal. In recent years, tools such as high numerical aperture objectives [1, 2, 3] and near-field scanning optical microscopy tips [4] have been used for both efficient photoluminescence (PL) collection and resonant optical spectroscopy.

A related problem is optical spectroscopy of microphotonic resonators, where wavelength-scale focusing and effective separation of the signal from background scattered light are also necessary. The optical fiber taper waveguide is a tool that has been investigated for such experiments. These structures, sometimes referred to as silica nanofibers, are standard single mode optical fibers that have been heated and stretched down to a wavelength-scale minimum diameter. At such small dimension, the evanescent field of the waveguide mode extends into the air

cladding and can be used to interrogate surrounding structures. By conducting the tapering process adiabatically and symmetrically, a double-ended device with standard single mode fiber input and output can be produced, with a typical overall transmission loss of less than 10 %. The combination of low loss, single mode guidance, and access to a wavelength-scale evanescent field has made tapered fiber probes invaluable for a wide number of microcavity-based experiments, including those in single atom and quantum dot cavity quantum electrodynamics [5, 6, 7]. These properties also suggest that they can be effective tools for single emitter spectroscopy. Indeed, theoretical work [8, 9] has indicated that silica nanofibers can be used to efficiently collect fluorescence from single gas phase atoms, and experimental progress to this end has been made [10].

The above studies indicate that optical fiber taper waveguides can be a general spectroscopic tool for nanophotonic systems, providing motivation for the present work. Here, we study their potential for efficient non-resonant and resonant fluorescence collection experiments on single solid state emitters embedded in a dielectric slab. Additional motivation is provided in previous experimental work [11], where a fiber taper waveguide was used in non-resonant PL measurements of a single InAs quantum dot embedded in a 256 nm thick GaAs membrane on top of an $\text{Al}_{0.7}\text{Ga}_{0.3}\text{As}$ pedestal. There, a luminescence collection efficiency of $\approx 0.1\%$ was estimated based on the measured saturated photon count rates, neglecting possible radiation rate modification due to the host structure, a non-resonant microdisk cavity, and any quantum dot non-idealities. Important questions left unanswered include how close this efficiency was to the theoretical maximum for the particular geometry considered, and how the geometry may be modified to lead to higher efficiencies. Furthermore, the possibility of studying resonant fluorescence, not addressed in [11], should also be considered. As described in other recent works [1, 2, 3, 4, 7, 12], resonant spectroscopy has advantages in comparison to non-resonant PL measurements in terms of greatly improved spectral resolution, potentially improved temporal resolution, the ability to avoid generation of decoherence-inducing excess carriers, well-defined state preparation, and possible utility in quantum information processing experiments.

To address these points, we consider the spontaneous emission of a dipole embedded in a semiconductor slab surrounded by air and in contact with a micron diameter silica optical fiber. Specifically, we envision an experimental measurement setup as depicted in Fig. 1, where the optical fiber taper waveguide is brought into close proximity with a thin semiconductor membrane hosting a single quantum emitter. The fiber has been adiabatically tapered to reach the single-mode condition over its central region (hundreds of microns long). The emitter may be optically pumped through an external fiber-coupled source, and radiates in both directions into the fiber, with a total coupling efficiency η_{PL} into the fundamental fiber mode (both backward and forward directions). We perform full wave, 3D finite difference time domain (FDTD) electromagnetic simulations of a single classical dipole radiating in the probing structure shown in Figs. 1(b)-1(c), and obtain the fiber-collected power. We find that fiber collection efficiencies in excess of $\approx 12\%$ (30%) may be achieved for dipole moments horizontally (vertically) oriented with respect to the membrane plane, exceeding what may be achieved with standard free-space optics PL collection schemes by an order of magnitude or more. These results suggest that optical fiber taper waveguides are potentially quite valuable in future studies of single solid state quantum emitters.

To determine ways of further improving collection efficiency, we analyze the dependence of both the modified spontaneous emission rate and PL collection efficiency on the electromagnetic supermodes of the probing structure. The starting point of our analysis is [8], which determines the modified spontaneous emission rate of a multi-level atom near a silica fiber. Addition of the semiconductor slab is a non-trivial modification of this problem, requiring the use of finite-element method (FEM) simulations to compute the guided and radiation modes

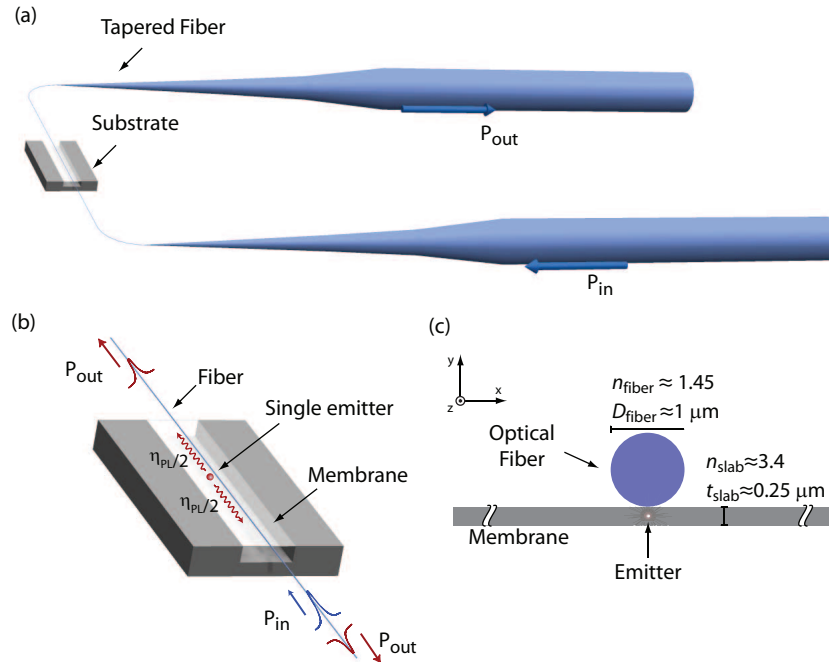


Fig. 1. (a) Single emitter probing setup based on a tapered fiber waveguide. (b) Detail of (a), showing the membrane that carries the emitter. (c) Schematic of the substrate cross-section, showing membrane and fiber.

of the composite slab-fiber system. These modes are used along with FDTD to determine the individual supermode contributions to the spontaneous emission fiber coupling fraction η_{PL} , under the assumption that the embedded emitter can be approximated as a two-level system.

The paper is organized as follows. In Section 2, we use FDTD to estimate the spontaneous emission collection efficiency into an optical fiber for a single quantum dot embedded in a semiconductor membrane, as shown in Fig. 1. The results of this section are analyzed in Section 3 in terms of the propagating supermodes of the probing structure. In Section 4, we further discuss the physical interpretation of these results and consider how they change with fiber size and if the host semiconductor membrane rests on a substrate (i.e., a non-undercut slab geometry). We also consider a pair of specific configurations with improved collection efficiencies, for which additional investigations are underway. Finally, we describe how resonant fluorescence measurements can be performed through our fiber-based probing and collection scheme.

2. Fiber-based embedded single emitter photoluminescence collection

In this section, we analyze the photoluminescence (PL) collection from a single emitter embedded in a dielectric slab with the fiber taper probe setup illustrated in Fig. 1. For non-resonant PL measurements, application of the fiber probe in the configuration of Fig. 2(a) is envisioned, which provides fiber-confined paths for excitation and PL collection in both forward and backward directions. As indicated in Fig. 1(b), the micron-scale single mode region of the optical fiber waveguide is brought into close proximity with the top surface of a dielectric membrane that hosts the emitter, over a length of several to hundreds of wavelengths. Fiber and membrane together form the composite dielectric waveguide with cross-section shown in Fig. 1(c). The

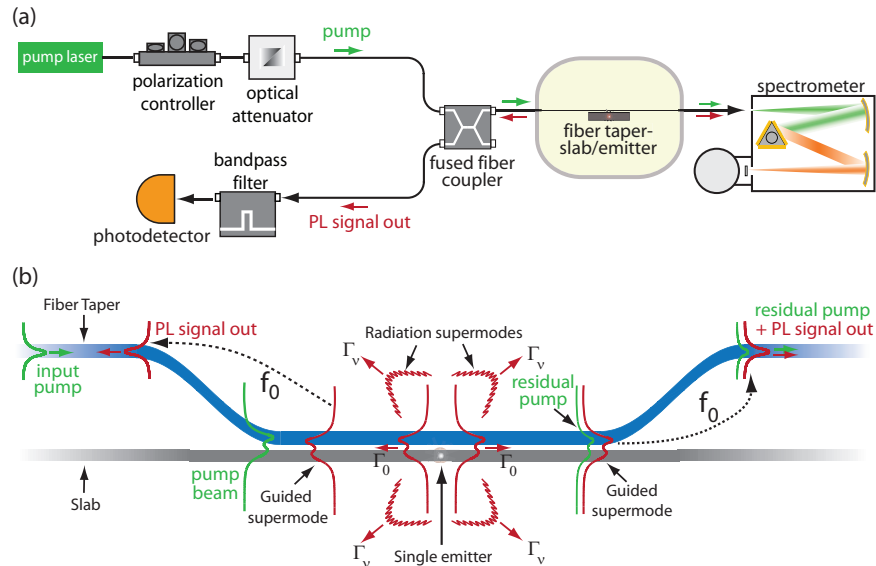


Fig. 2. (a) Envisioned experimental configuration for fiber-based non-resonant photoluminescence (PL) spectroscopy with a tapered fiber waveguide. Emitted light is coupled into both forward and backward channels of the fiber taper waveguide, and can be wavelength resolved with a grating spectrometer or spectral filter. (b) Schematic of single emitter excitation and PL collection via the tapered fiber probe. A non-resonant pump signal is injected into the input fiber and converted into a guided supermode of the composite waveguide, illuminating the slab-embedded dipole. The dipole radiates into guided and radiative supermodes, with rates Γ_0 and Γ_v , respectively. Power is transferred with efficiency f_0 from the supermode to the fiber mode and vice-versa.

composite waveguide supports a complete set of guided, leaky and radiation supermodes [13], originating from the hybridization of fiber and slab modes. As depicted in Fig. 2(b), part of the non-resonant pump power initially carried by the fiber is coupled to a guided supermode of the composite waveguide and transferred toward the emitter. Illuminated by the pump light, the emitter radiates (at a red-shifted wavelength) into modes of the composite fiber-slab waveguide. Our objective is to determine the fraction of this emission that would be measured at the single mode fiber output, after the micron-scale fiber has transitioned away from the slab. The portion of the total emission collected by the fiber is carried by those supermodes with sufficient transverse confinement to reach the fiber transition regions with significant amplitude. Thus, apart from guided modes, leaky modes may contribute significantly to the total PL collection.

Within this scenario, we estimate the spontaneous emission collection efficiency for a single emitter in a geometry that approximates the tapered-fiber-based quantum dot spectroscopy setup of [11]. In that work, PL spectroscopy of single self-assembled InAs quantum dots embedded in a non-resonant 256 nm thick GaAs microdisk was demonstrated, with an estimated collection efficiency of 0.1 % (including both channels of the optical fiber). Our numerical estimate here is obtained through full electromagnetic simulations of a point dipole radiating inside the composite waveguide of Fig. 1(c). The geometry consists of a dielectric slab of index $n_{\text{slab}} = 3.406$, and fiber of radius $r = 500\text{ nm}$ and refractive index $n_{\text{fiber}} = 1.45$ placed directly on the top surface of the slab. The dipole is assumed to radiate at $\lambda = 1.3\text{ }\mu\text{m}$, a wavelength at which the fiber possesses, apart from the fundamental guided mode, a near-cutoff mode which is not significant in our calculations. Slab membranes of thicknesses varying between 100 nm and 260 nm were investigated, sufficient to avoid quantum dot dephasing due to surface-state-related processes, as suggested in [14]. In Section 4, we consider how these results change when

r is decreased to 300 nm and when the slab membrane is placed directly on a substrate.

2.1. Simulation Method

To estimate the PL collection efficiency of our fiber-based probing scheme, we considered a single classical electric dipole radiating in the composite dielectric waveguide of Fig. 1(c). An upper bound for the percentage of the total emitted power $P_{\text{Tot.}}$ coupled to the fundamental optical fiber mode at an arbitrary position z along the guide is

$$\eta_{\text{PL}} = 2 \frac{P_z}{P_{\text{Tot.}}} f_{\text{fiber}}, \quad (1)$$

where P_z is the power flowing normally through the constant- z plane, and f_{fiber} is the overlap integral [15]

$$f_{\text{fiber}} = \frac{\text{Re} \left\{ \iint_S (\mathbf{e}_f \times \mathbf{h}^*) \cdot \hat{\mathbf{z}} dS \iint_S (\mathbf{e} \times \mathbf{h}_f^*) \cdot \hat{\mathbf{z}} dS \right\}}{\text{Re} \left\{ \iint_S (\mathbf{e}_f \times \mathbf{h}_f^*) \cdot \hat{\mathbf{z}} dS \right\} \text{Re} \left\{ \iint_S (\mathbf{e} \times \mathbf{h}^*) \cdot \hat{\mathbf{z}} dS \right\}}. \quad (2)$$

Here, $\{\mathbf{e}, \mathbf{h}\}$ are the steady-state radiated fields at position z and $\{\mathbf{e}_f, \mathbf{h}_f\}$ the fundamental fiber mode fields. The factor of 2 in Eq. (1) is introduced to account for collection from both fiber ends.

The steady-state fields were obtained through FDTD simulations [16]. The symmetry of the geometry allowed us to choose either anti-symmetric ($\hat{\mathbf{x}} \times \mathbf{E} = 0$) or symmetric ($\hat{\mathbf{x}} \times \mathbf{H} = 0$) boundary conditions on the yz -plane, the former being used for x -polarized dipoles, and the latter for y - and z -polarized dipoles. The computational domain was cubic with a $10 \mu\text{m}$ side and perfectly-matched layers (PMLs) were used around the domain limits to simulate an open domain. Dipole excitation consisted of a $\lambda = 1.3 \mu\text{m}$ carrier modulated with a 0.1 nm bandwidth gaussian envelope. Simulations ran until no field amplitude could be detected in the domain. The total radiated power $P_{\text{Tot.}}$ was calculated by adding the integrated steady-state power through all the computational window sides. The PL collection efficiency η_{PL} was calculated at several z -planes along the propagation direction (z) in the computational domain.

2.2. Simulation Results

2.2.1. Total radiated power

Figure 3(a) shows the FDTD-calculated, total radiated power ($P_{\text{Tot.}}$) for x -, y - and z -oriented dipoles located at the slab center in the structure of Fig. 1(c). The curves were normalized to the total radiated power of an electric dipole current source $\mathbf{J}(\mathbf{r}, t) = -i\omega \mathbf{p} \delta(\mathbf{r}) e^{-i\omega_0 t}$ in a homogeneous dielectric medium of refractive index n_{slab} and electric dipole moment \mathbf{p} [17]:

$$P_{\text{Hom.}} = \frac{\mu_0}{4\pi} n_{\text{slab}} |\mathbf{p}|^2 \frac{\omega_0^4}{3c}. \quad (3)$$

The total radiated power is not significantly different when the fiber is absent. This is evident in Fig. 3(b), where the power radiated by vertical or horizontal dipoles into modes of an isolated slab are plotted. These curves were calculated using the transfer-matrix method of [18]. Transverse-electric waves (TE) have electric field components in the slab plane only, while transverse-magnetic (TM) modes have only in-plane magnetic field components. As a result, a vertical (y -directed) dipole excites only TM waves, while horizontal (x - and z -directed) dipoles can excite both TE and TM waves [18], although as we see in Fig. 3(b), the TE mode excitation is much more significant. The similarity between the total radiated power curves for the slab with or without the fiber indicates its weak perturbative effect on the emission, so we first proceed by analyzing the isolated slab. Figure 4(a) displays the effective indices

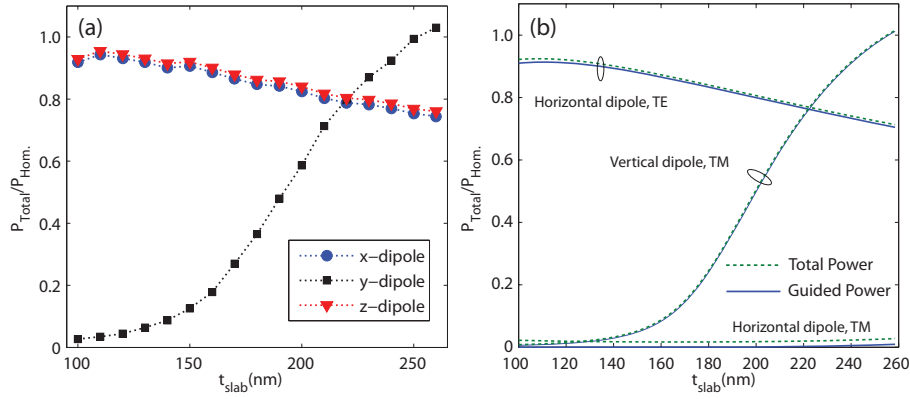


Fig. 3. (a) Total radiated power at $\lambda = 1.3 \mu\text{m}$ for a dipole in the composite slab-fiber waveguide, normalized to the radiated power in a homogeneous medium of index n_{slab} . (b) Guided and total radiated powers into TE (TM) waves for a horizontal (vertical and horizontal) dipole at the center of a dielectric slab with $n_{\text{slab}} = 3.406$.

of the TE_0 , TE_1 and TM_0 modes, for varying slab thickness. The evolution of the field concentration at the dipole for both TE and TM modes may be inferred from the effective length, $L_{\text{eff}} = \int \epsilon |\mathbf{E}|^2 dy / |\mathbf{E}(\mathbf{r}_0)|$, where \mathbf{r}_0 is the dipole position, plotted in Fig. 4(b). The effective length is inversely proportional to the dipole power coupled to the mode [19, 20].

Given the large refractive index of the slab relative to air, total internal reflection leads to preferential dipole excitation of guided waves. This is verified in the curves for guided and total radiated powers in Fig. 3(b) [18]. For a horizontal dipole at the slab center, most of the radiated power is carried by the TE_0 mode, which has a relatively small effective length, L_{eff} . The TE_1 mode is not excited, since its electric field has a node at the dipole location. The TM_0 mode is also not excited, as $\mathbf{E}_x = 0$ and \mathbf{E}_z has a null at the slab center. For a vertical dipole, excitation of the TM_0 mode is more effective, especially since no TE modes are generated [18]. The strong emission inhibition for vertical dipoles at small t_{slab} is due to poor outcoupling into the air, resulting from total internal reflection, and poor field concentration, apparent in the large TM_0 effective lengths L_{eff} of Fig. 4(b). As a result, even if high fiber collection efficiencies can be achieved, this strong suppression of spontaneous emission can lead to low overall photon count rates at the detector.

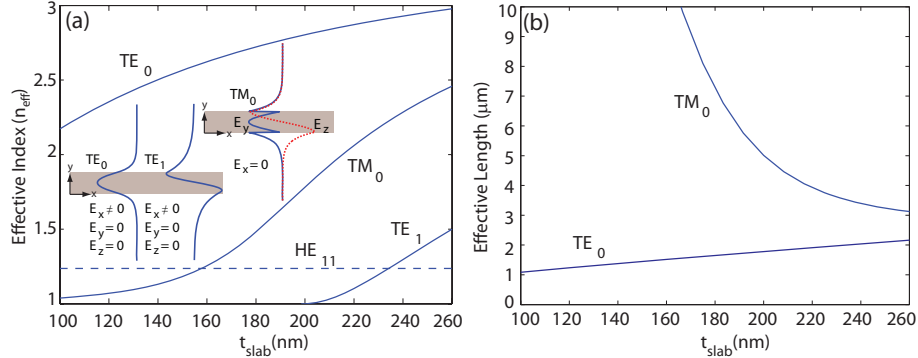


Fig. 4. (a) Effective indices of the slab TE_0 , TE_1 and TM_0 modes at $\lambda = 1.3 \mu\text{m}$. The HE_{11} fiber mode effective index is also shown. Inset: field components of TE_0 , TE_1 and TM_0 slab modes. (b) Effective lengths, L_{eff} , for the TE_0 and TM_0 slab modes.

2.2.2. Photoluminescence Collection

Using Eq. (1), the collection efficiency η_{PL} was calculated for a range of propagation lengths a few wavelengths away from the dipole location ($1\ \mu\text{m} < z < 5\ \mu\text{m}$). The results reveal strong periodic oscillations as a function of this distance, as shown in the inset of Fig. 5(a). As we shall discuss in the following section, this oscillation is due to the beating of two principal waveguide supermodes with distinct propagation constants, corresponding to the sloshing of power between fiber and slab, as commonly observed in coupled waveguide systems [15]. Oscillations in η_{PL} are accompanied by a decrease in its peak value - as we shall see in Section 3, this decay is due to leaky modes with propagations lengths of several wavelengths. The maximum and minimum values of η_{PL} within the simulated propagation range were taken to generate the PL efficiency plots for x -, y - and z -directed dipoles of Fig. 5. Note that the values plotted in Fig. 5 include collection through both the forward and backward channels of the fiber, an experimentally viable situation through use of a fused fiber coupler (Fig. 2(a)).

We first consider the results for in-plane oriented dipoles (in the x and z directions), which are of relevance to quantum dot experiments such as in [11]. For x -oriented dipoles, the maximum collection efficiency ranges from $\approx 7\%$ to $\approx 2\%$ for t_{slab} varying from 100 nm to 260 nm, while the minimum efficiencies remain close to 0.1 % throughout. For z -oriented dipoles, the efficiency varies below 1 % for all thicknesses. In [11], a single quantum dot inside a 256-nm GaAs slab was probed, and a measured collection efficiency of 0.1 % was estimated. This value is within the limits predicted by Figs. 5(a) and 5(c), given that the in-plane dipole orientation was not known, and the quantum dot was assumed to have unity radiative efficiency. In addition, the in-plane position of the quantum dot was such that the underlying $\text{Al}_{0.7}\text{Ga}_{0.3}\text{As}$ support pedestal could have had significant influence on the PL collection. We consider its effects in Section 4.

To further gauge our current results, we use the method of [18] to plot, in Fig. 5, the maximum achievable free-space collection efficiency for a dipole embedded in the slab (without the fiber), using a 0.7 numerical aperture (NA) objective. We see that the maximum achievable η_{PL} for horizontally-oriented dipoles in the fiber-based collection scheme is superior to the

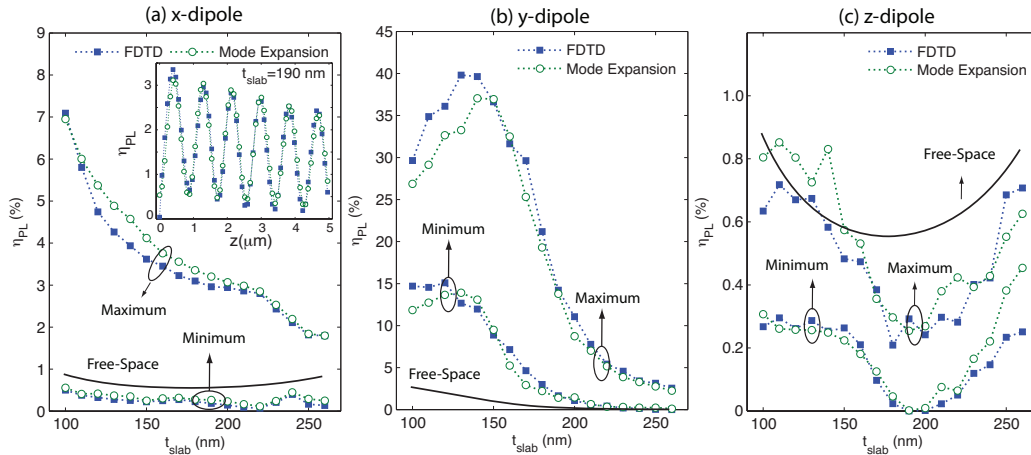


Fig. 5. Fiber-collected PL coupling efficiency η_{PL} for (a) x -, (b) y - and (c) z - oriented dipoles at $\lambda = 1.3\ \mu\text{m}$. Collection through both the forward and backward fiber channels is considered (notice changing axis scales). Since η_{PL} oscillates with z , its maximum and minimum along $z < 5\ \mu\text{m}$ are plotted. The inset in (a) shows η_{PL} as function of z . Squares: FDTD results. Circles: Mode-expansion results. Solid lines: Free-space collection efficiency considering a NA=0.7 objective.

free-space collection efficiency by as much as an order of magnitude, as indicated in Fig. 5(a). As is the case with other co-propagating waveguide directional couplers [15], control of the interaction length is necessary to achieve the most efficient power transfer. Here, to obtain the highest values of η_{PL} , one might envision controlling the length of the membrane through standard planar fabrication techniques. Alternately, the effective fiber-membrane interaction region can be limited using 'dimpled' fiber taper waveguides [21]. Given the low propagation losses in the optical fiber and a typical insertion loss of 10 % through the taper, the present technique constitutes a competitive option for PL spectroscopy.

For vertically oriented dipoles, the collection efficiency may reach above 35 % at $t_{\text{slab}} = 140\text{nm}$, where the dipole emission is strongly suppressed. For thicker slabs, the suppression is reduced, but the collection efficiency drops, reaching $\approx 3\%$ for $t_{\text{slab}} = 250\text{nm}$. Even this collection efficiency is nonetheless an order of magnitude higher than what may be obtained with free-space collection with a 0.7-NA objective, plotted in Fig. 5(b). Although self-assembled quantum dots in semiconductor slabs are typically in-plane oriented dipoles, we note that manipulation of the quantum dot growth can change its shape sufficiently to produce structures that support TM-polarized emission [22]. The results presented here would be of significant interest to such systems.

While the results presented in this section are analyzed in detail in Section 3, we provide here a brief explanation for the relatively high collection efficiencies found, regarding the fiber-slab system as a directional coupler. In a directional coupler, power transfer takes place between waves, in respective waveguides, of similar propagation constants. Although transfer is most efficient when both waves are perfectly matched, small but significant transfer may still occur between mismatched modes. As discussed in Section 2.2.1, most of the x-polarized dipole radiation is carried by TE slab mode waves. A significant portion of these waves, though phase-mismatched to the fiber mode, transfer small amounts of power to the latter, collectively leading to relatively high (8 % maximum) collection efficiencies. The substantially higher (40 % maximum) collection efficiency obtained for y-oriented dipoles results from a more effective power transfer from TM slab waves to the fiber mode: phase matching between the fiber and TM_0 slab modes is apparent in Fig. 4(a), for slab thicknesses close to 160nm.

3. Analysis

While the FDTD simulations provide estimates of the total spontaneous emission rate and fiber-coupled collection efficiency, they do not necessarily provide physical understanding of effects such as the oscillation and decay in PL collection efficiency as a function of separation from the dipole in the propagation direction, or the insight needed to extend this work to modified geometries. In this section, we address these issues through FEM simulations that determine the modal structure of the composite fiber-slab system. This allows us to determine the spontaneous emission rate, and contribution to the total collected PL, of individual supermodes of the system. This approach furthermore allows us to estimate the evolution of the coupling efficiency for coupling lengths much longer than practical in FDTD simulations.

3.1. Supermodes of the composite waveguide

The composite waveguide of Fig. 1 supports a set of hybrid supermodes of the fundamental, micron-scale fiber mode and the bound, TE_m ($E_y = 0$) or TM_m ($H_y = 0$) slab modes. These supermodes are henceforth referred to as hybrid- TE_m or hybrid- TM_m . The fiber creates a region of increased effective refractive index on the slab plane, spanning a discrete set of laterally confined hybrid-TE or hybrid-TM supermodes. A continuum of radiation hybrid-TE or hybrid-TM supermodes also exists, which represents waves not laterally confined by the increased fiber-induced effective index. A portion of this radiative supermode spectrum corresponds to optical

power that, although unconfined, lingers near the fiber for relatively long propagation distances (tens of wavelengths), and may contribute significantly to the PL collection efficiency. These wave bundles may be represented by a discrete set of leaky supermodes, which extend infinitely in the lateral direction and decay in the propagation direction [13]. The relevant waves for PL collection within our scheme are thus the guided and leaky hybrid-TE or hybrid-TM supermodes.

The supermode field distributions of our structure were obtained through the vector eigenvalue problem for the magnetic field \mathbf{H}

$$\nabla \times \left(\frac{1}{\varepsilon(\mathbf{r})} \nabla \times \mathbf{H} \right) - \left(\frac{\omega}{c} \right)^2 = 0. \quad (4)$$

Here, $\mathbf{H} = \mathbf{H}(\mathbf{r}) \exp(\xi z)$, and $\xi = i\beta - \alpha_z = i\omega n_{\text{eff}}/c$ is a complex propagation constant with a phase term β and a decay term α_z , or equivalently a complex effective index n_{eff} . The number of free-space wavelengths necessary for the supermode amplitude to decay by a factor $0 < \delta < 1$ is $N_\delta = -n_i^{-1} \ln(\delta)/2\pi$, where $n_i^{-1} = \text{Im}\{n_{\text{eff}}\}^{-1}$. This number is used in our analysis to roughly determine the probing length (i.e., the length over which the fiber contacts the slab) for supermode power collection to be most effective. Since the dipole is aligned with the center of the fiber, the problem is symmetric with respect to the yz plane. An x -oriented dipole thus only excites hybrid-TE supermodes, for which $\hat{\mathbf{x}} \times \mathbf{E} = 0$ on the symmetry plane. Conversely, y - and z -oriented dipoles only excite hybrid-TM supermodes, for which $\hat{\mathbf{x}} \times \mathbf{H} = 0$ on the yz plane.

The isolated slab waveguide supports a TE_0 and a TM_0 mode for all slab thicknesses t_{slab} considered, and a TE_1 mode for $t_{\text{slab}} \gtrsim 200 \text{ nm}$ (Fig. 4), so that the composite waveguide structure supports hybrid- TE_0 and hybrid- TM_0 and hybrid- TE_1 modes in the same ranges. Field profiles for the strongest-confinement hybrid- TE_0 and hybrid- TM_0 supermodes are shown in Figs. 6(a) and 6(d) of Section 3.5.

3.2. Modified spontaneous emission rate in the composite waveguide

To describe the spontaneous emission of a single quantum emitter into the composite dielectric waveguide of Fig. 1 in terms of its supermodes, we begin by making use of [8], where the spontaneous emission rate of a multi-level atom into the guided and radiative modes of a silica optical fiber are calculated. These expressions are derived from the Heisenberg equations for a multilevel atom experiencing a dipole-type interaction with a vacuum field reservoir that is described in terms of propagating waveguide modes. While [8] focused exclusively on optical fibers, here we deal with general dielectric waveguides, so that the expressions we use are modified accordingly from their originals, with the derivation presented in Appendix B.

The waveguide, extending in the z direction, is open, and thus supports a finite set of guided modes and a continuum of unconfined, radiation modes [13]. Guided modes and radiation modes are respectively labeled with the indices μ and ν , and have propagation constants β_μ and β at frequency ω . For the radiation mode continuum, β may assume any value in the interval $|\beta| < \omega n/c$, where n is the refractive index of the medium surrounding the waveguide. Evanescent radiation modes are excluded, as they do not participate in the radiation process [23].

For a two-level atom located in a general dielectric waveguide at a position \mathbf{r}_0 , with a transition of energy $\hbar\omega_0$ and dipole moment \mathbf{p} , the spontaneous emission rates into guided and radiative modes are, respectively, $\Gamma_\mu = 2\pi|G_\mu(\omega_0)|^2$ and $\Gamma_\nu = 2\pi|G_\nu(\omega_0)|^2$, where

$$G_\mu = \sqrt{\frac{\omega\beta'_\mu}{4\pi\varepsilon_0\hbar}} [\mathbf{p} \cdot \mathbf{e}_\mu(\mathbf{r}_0)] \quad \text{and} \quad G_\nu = \sqrt{\frac{\omega}{4\pi N_\nu \hbar}} [\mathbf{p} \cdot \mathbf{e}_\nu(\mathbf{r}_0)]. \quad (5)$$

Here, \mathbf{e}_μ and \mathbf{e}_ν are the electric fields of the guided and radiative modes, with respective propagation constants β_μ and β . Also, $\beta'_\mu = \partial\beta_\mu/\partial\omega$ and N_ν is such that [13]

$$\iint_S dS (\mathbf{e}_\nu \times \mathbf{h}_{\nu'}^*) \cdot \hat{\mathbf{z}} = N_\nu \delta(\beta - \beta'). \quad (6)$$

Guided and radiative modes are normalized so that

$$\iint_S dS \varepsilon(\mathbf{r}) |\mathbf{e}_\mu|^2 = 1 \quad (7)$$

$$\iint_S dS \varepsilon(\mathbf{r}) (\mathbf{e}_\nu \cdot \mathbf{e}_{\nu'}^*)_{\beta=\beta', n=n'} = \delta(\omega - \omega') \quad (8)$$

where S is the cross-section of the waveguide and $\varepsilon(\mathbf{r})$ the spatial permittivity distribution. The total emission rate is

$$\Gamma = \sum_\mu \Gamma_\mu + \sum_n \int d\beta \Gamma_\nu. \quad (9)$$

According to Eq. (A-8), the power emitted from a classical dipole into a particular mode depends on the modal electric field concentration at the dipole position (the modal electric fields are normalized to the power density flux integrated over the waveguide cross-section). We introduce the effective area $A_{\text{eff}} = \int \varepsilon |\mathbf{E}|^2 dS / |\mathbf{E}(\mathbf{r}_0)|^2$ as a measure of the field concentration at the emitter position. This expression is implicit in the modal rates of Eq. (5), given the normalization expressions, Eqs. (7) and (8). The total spontaneous emission rate, being the sum of the individual modal rates, deviates considerably from the free-space rate if highly concentrated modes (i.e., small effective areas) exist at the emitter location.

To avoid calculation of all radiative modes of the composite waveguide, the spontaneous emission rate Γ was obtained through the following relationship between the spontaneous emission rates for an emitter in a homogeneous medium ($\Gamma_{\text{Hom.}}$) and into a waveguide (Γ_{WG}), and the total classical dipole radiated powers in bulk ($P_{\text{Hom.}}$) and in a waveguide (P_{WG}) [13]:

$$\frac{\Gamma_{\text{WG}}}{\Gamma_{\text{Hom.}}} = \frac{P_{\text{WG}}}{P_{\text{Hom.}}} \quad (10)$$

The validity of this expression is demonstrated in Appendix A (a similar relation for cavities has been established in [24]). This equivalence allowed us to use FDTD simulations to determine total spontaneous emission rates.

3.3. Photoluminescence Collection

With the help of Eq. (10), we may describe the electric and magnetic fields radiated by a dipole located at $z = 0$ inside the slab in terms of traveling supermodes. At an arbitrary z -plane along the waveguide direction, $\mathbf{e} = \sum_{m=1}^M \sqrt{\Gamma_m/\Gamma} \mathbf{e}_m \exp(i\xi_m z)$ and $\mathbf{h} = \sum_{m=1}^M \sqrt{\Gamma_m/\Gamma} \mathbf{h}_m \exp(i\xi_m z)$, where \mathbf{e}_m and \mathbf{h}_m are the fields of the m -th eigensolution of Eq. (4), with eigenvalue $\xi_m = \beta_m + i\alpha_{z,m}$. The factor Γ_m is the supermode emission rate from Eq. (5). Applied in Eq. (2), these fields lead to the following expression for the percentage of the total spontaneous emission carried by the fiber mode:

$$\eta_{PL} = 2 \sum_{m=1}^M f_m \frac{\Gamma_m}{\Gamma} + 2 \sum_{\substack{m,n=1 \\ m \neq n}}^M \sqrt{\frac{\Gamma_m}{\Gamma}} \sqrt{\frac{\Gamma_n}{\Gamma}} \text{Re} \left\{ \sqrt{f_m^h f_n^e} \exp[i(\xi_m - \xi_n^*)z] \right\}, \quad (11)$$

where

$$\sqrt{f_m^h} = \frac{\iint_S (\mathbf{e}_f \times \mathbf{h}_m^*) \cdot \hat{\mathbf{z}} dS}{\sqrt{\text{Re} \{ \iint_S (\mathbf{e}_m \times \mathbf{h}_m^*) \cdot \hat{\mathbf{z}} dS \} \text{Re} \{ \iint_S (\mathbf{e}_f \times \mathbf{h}_f^*) \cdot \hat{\mathbf{z}} dS \}}}, \quad (12)$$

$$\sqrt{f_m^e} = \frac{\iint_S (\mathbf{e}_m \times \mathbf{h}_f^*) \cdot \hat{\mathbf{z}} dS}{\sqrt{\text{Re} \{ \iint_S (\mathbf{e}_m \times \mathbf{h}_m^*) \cdot \hat{\mathbf{z}} dS \} \text{Re} \{ \iint_S (\mathbf{e}_f \times \mathbf{h}_f^*) \cdot \hat{\mathbf{z}} dS \}}}, \quad (13)$$

and $f_m = \text{Re} \left\{ \sqrt{f_m^h} \sqrt{f_m^e} \right\}$. The factor of 2 is introduced to account for collection from both fiber ends. While the first sum in Eq. (11) corresponds to the individual supermode contributions to η_{PL} , the latter corresponds to beating of the individual supermode field components. These contributions, which may be substantial, are periodic in z , with beat lengths $L_z = 2\pi/(\beta_m - \beta_n)$, where $\beta_{m,n}$ are the m -th and n -th supermode propagation constants. The m -th supermode individual contribution to the spontaneous emission collection efficiency is $\eta_{PL,m} = f_m \cdot (\Gamma_m/\Gamma) = f_m \gamma_m$. The ratio $\gamma_m = \Gamma_m/\Gamma$ gives the fraction of spontaneous emission coupled into the supermode. Reflecting the fact that supermodes in our structure are hybrids of the fundamental fiber mode and slab TE and TM modes, f_m is called the fiber-mode fraction of the m -th supermode.

The estimate of $\eta_{PL,m}$ could be improved through a more detailed consideration of the transition between fiber-slab supermode and fundamental fiber mode. In the case of an abrupt transition (e.g., if the membrane is terminated at cleaved facets), modal reflection and transmission coefficients may be obtained through rigorous wave matching at the interface, yielding the power transferred to the isolated fiber mode [15]. On the other hand, a power transfer in excess of 90 % is estimated from the Fresnel reflection and transmission coefficients at such an interface, considering the supermode and fiber effective indices. Transmission levels of this magnitude were confirmed in FDTD simulations of a truncated slab of thickness 190 nm, for dipoles placed at several distances from the transition. This suggests that the mode overlap method used here and in the previously presented FDTD results yields reasonable upper-bound estimates for the achievable collection efficiency.

3.4. Supermode Calculation Method

The eigenvalue equation Eq. (4) was solved with FEM with quadratic vector elements for \mathbf{H}_x and \mathbf{H}_y and Lagrange elements for \mathbf{H}_z [25]. Given the symmetry of the problem, only half of the geometry was considered, with either anti-symmetric ($\hat{\mathbf{x}} \times \mathbf{E} = 0$) or symmetric ($\hat{\mathbf{x}} \times \mathbf{H} = 0$) boundary conditions on the y -axis, which automatically selected either hybrid-TE or hybrid-TM solutions. Perfectly-matched layers were defined over the outer boundaries to simulate an open domain, as leaky modes were expected. Perfect electric conductor ($\hat{\mathbf{n}} \times \mathbf{E} = 0$) boundary conditions surround the PML on the outermost boundaries. The eigenvalue calculation produced a finite, discrete set of supermode solutions, which were used in Eq. (11) to estimate η_{PL} . The respective emission rates Γ_m were calculated with the guided-mode expression in Eq. (5). In all our calculations, fifty supermodes were used, which was sufficient to closely reproduce the FDTD results.

3.5. Simulation results

The PL collection efficiencies for x -, y - and z -dipoles calculated with the supermode expansion method above are plotted in Fig. 5. The discrepancies in the y - and z dipole cases relative to the FDTD results are largely due to an insufficiently fine grid used in the FDTD simulations, where a full 3D simulation is run. In the FEM simulations, a cross-section of the structure is analyzed

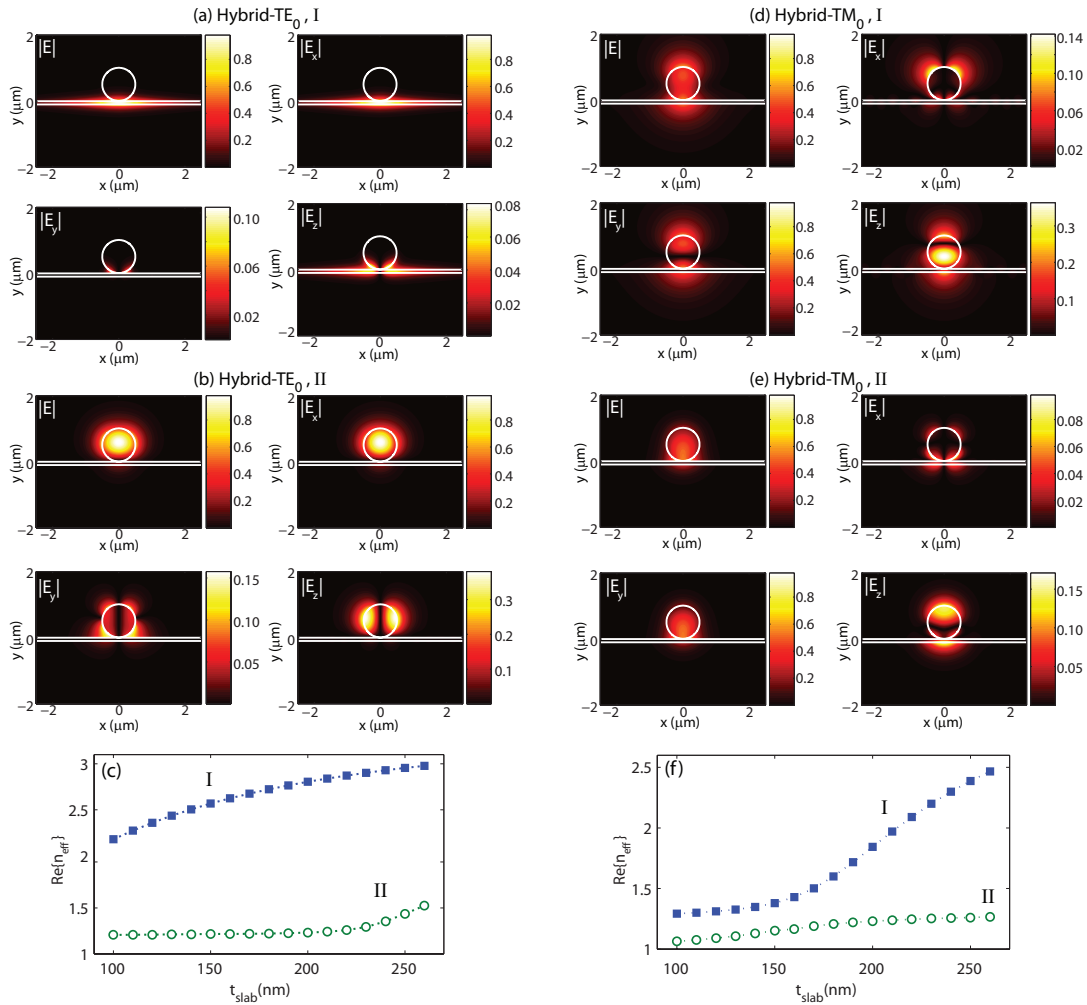


Fig. 6. Electric field distribution for (a), (b): hybrid-TE₀ types-I (slab-like) and II (fiber-like) supermodes; (d), (e): hybrid-TM₀ types-I and II supermodes. Fields are for $t_{\text{slab}} = 100\text{nm}$ and $\lambda = 1.3\mu\text{m}$. (c) and (f): effective indices for (c) hybrid-TE₀ and (f) hybrid-TM₀ supermodes of types I and II for varying t_{slab} . Fields have been normalized to the total field amplitude maxima in each case. Color scales are in arbitrary units.

and hence can be discretized with a finer resolution. As discussed below, the main hybrid-TM modes, excited by either y - or z -dipoles, are strongly concentrated in the region between fiber and slab, requiring a very fine grid for high accuracy. To avoid prohibitively long computation times, a coarser grid was used.

Hybrid TE modes: x -oriented dipoles

Figure 7(a) shows a representative effective index distribution for hybrid-TE supermodes. For x -oriented dipole excitation, the two supermodes labeled I and II have the largest contribution to the total collected PL. Types-I and II supermodes are mostly concentrated in the slab and fiber regions respectively, and are thus referred to as slab-like and fiber-like. Representative electric-field profiles for these main supermodes are shown in Figs. 6(a) and 6(b), while Fig. 6(c) shows $\text{Re}\{n_{\text{eff}}\}$ as a function of t_{slab} for these modes. The periodic oscillation of η_{PL} with z , observed in the FDTD simulations, is very well reproduced by the mode expansion calculations, as shown

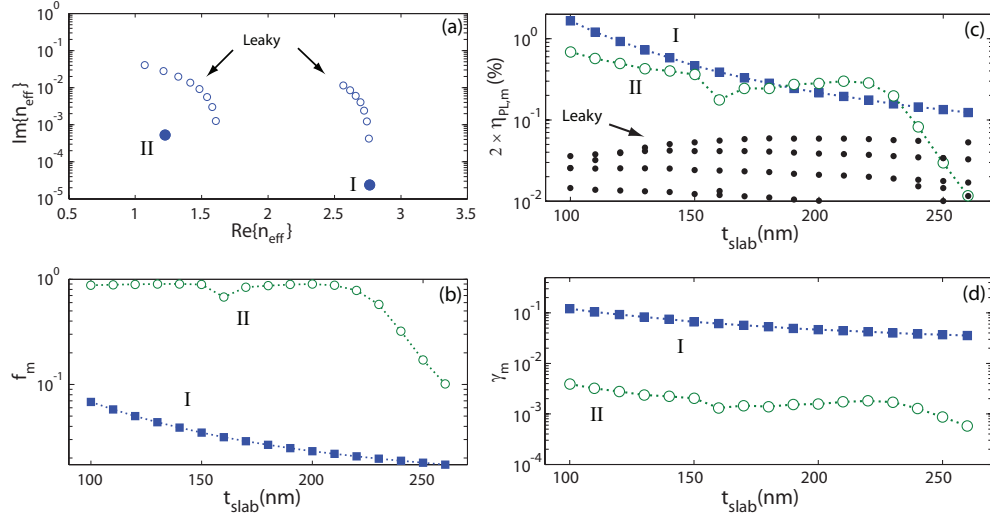


Fig. 7. (a) Effective indices for hybrid-TE supermodes at $t_{\text{slab}} = 190 \text{ nm}$ and $\lambda = 1.3 \mu\text{m}$. The two supermodes with highest modal emission rates are indicated with filled circles labeled I and II, corresponding to slab-like and fiber-like modes. Open circles indicate leaky modes. (b) Fiber fractions for supermodes I and II. (c) PL collection contributions from the individual supermodes, for an x -oriented dipole moment. The factor of 2 is to account for collection from both fiber ends. Black dots are for leaky modes. (d) Modal emission ratios for supermodes I and II. Filled squares/empty circles are for type I/II supermodes.

in the inset of Fig. 5(a). This oscillation is due to the beating of the two main supermodes, and persists when leaky eigenmodes are excluded from the calculation. The beat length is given by $L_z = 2\pi/(\beta_I - \beta_{II})$, where $\beta_{I,II}$ are the respective propagation constants.

The supermode power contributions, $\eta_{\text{PL},m}$, are shown in Fig. 7(c). The slab-like supermode is dominant for $t_{\text{slab}} \lesssim 160 \text{ nm}$ and $t_{\text{slab}} \gtrsim 240 \text{ nm}$, being surpassed by the fiber-like mode at intermediate thicknesses. In this range, the fiber-like supermode's significantly larger fiber fraction (Fig. 7(b)) is enough to compensate for its much lower modal emission ratio $\gamma_{0,II}$ (Fig. 7(d)). Individually, leaky supermodes pointed out in Fig. 7(a) add little to the total collected power, however their aggregate influence is non-negligible: excluding leaky modes, the maximum collected power drops between 40 % and 70 %, a significant portion of the total collected PL.

Among the leaky modes with $\eta_{\text{PL},m}$ above 1 % of the slab-like supermode contribution, the one with the lowest individual contribution has $n_i^{-1} \lesssim 156$, corresponding to $N_{\delta=0.9} \gtrsim 2.6$ wavelengths for 90 % amplitude decay. As a result, the highest efficiency collection shown in Fig. 5(a) will be achieved for coupling lengths of a few microns; the contribution from leaky modes will begin to drop out as the coupling lengths increase beyond this. The slab- and fiber-like supermodes have $N_{\delta=0.9} \gtrsim 427$ and $N_{\delta=0.9} \gtrsim 22$, respectively, so that a coupling length of $\lesssim 30 \mu\text{m}$ continues to allow collection of PL coupled to both main supermodes. Finally, collection that is at least as high as the slab-like supermode's contribution in Fig. 7(a) is achievable for lengths shorter than $550 \mu\text{m}$. We note that this latter result is still on par with what can be achieved through free-space collection (Fig. 5(a)).

Hybrid TM modes: y - and z -oriented dipoles

Figure 8(a) shows a representative effective index distribution for hybrid-TM supermodes, taken at a slab thickness $t_{\text{slab}} = 190 \text{ nm}$ that is in the middle of the simulation range. For

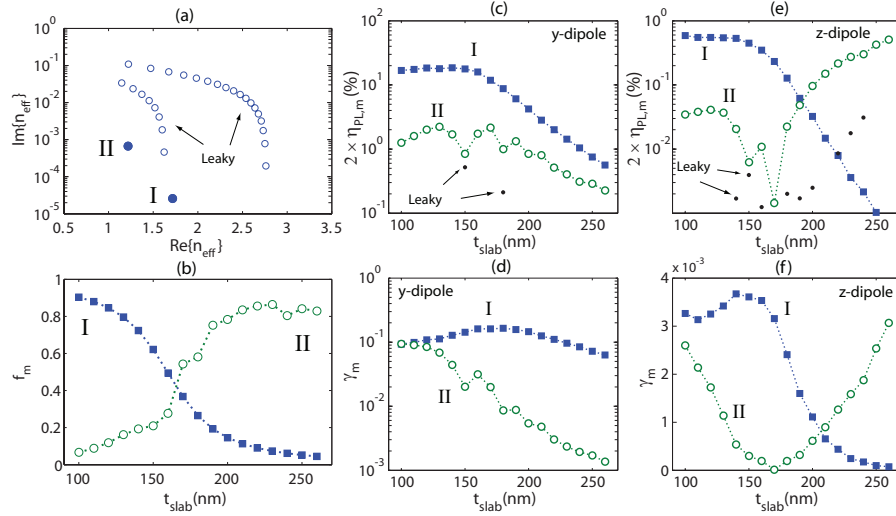


Fig. 8. (a) Effective indices for hybrid-TM supermodes at $t_{\text{slab}} = 190 \text{ nm}$ and $\lambda = 1.3 \mu\text{m}$. The two supermodes with highest modal emission rates are indicated with filled circles labeled I and II. Open circles indicate leaky modes. (b) Fiber fractions for supermodes I and II. (c) and (e): PL collection contributions from individual supermodes, for y- and z-oriented dipole moments respectively (notice changing axis scales). The factor of 2 is to account for collection from both fiber ends. (d) and (f): Modal emission ratios, for y- and z-oriented dipole moments of type-I and type-II supermodes (notice changing axis scales). Filled squares/empty circles are for type I/II supermodes; black dots are for leaky modes.

both y- and z- dipole excitation, two supermodes, labeled I and II, have the largest contribution to the total collected PL. Representative electric-field profiles and $\text{Re}\{n_{\text{eff}}\}$ for these main supermodes are shown in Figs. 6(d), 6(e) and 6(f). The type-I supermode is well confined, having the lowest $\text{Im}\{n_{\text{eff}}\}$, typically an order of magnitude lower than its type-II counterpart and all additional leaky modes. Leaky supermodes, pointed out in Fig. 8(a), provide a very small contribution to the collected PL, typically at least two orders of magnitude lower than the supermode with the largest contribution to η_{PL} . The type-I supermode is mostly concentrated in the fiber for small t_{slab} , and in the slab at larger thicknesses, as apparent in its fiber fraction plotted in Fig. 8(b). The type-II supermode resides mostly in the fiber region for all slab thicknesses, although its fiber-fraction increases with t_{slab} .

The individual supermode contributions $\eta_{\text{PL},m}$ to the total PL collection for a y-dipole are plotted in Fig. 8(c). The type-I supermode contribution dominates at all thicknesses, while most leaky mode contributions range below 10^{-3} . Its modal emission ratio is maximized for $t_{\text{slab}} \lesssim 200 \text{ nm}$ (Fig. 8(d)), for which a strong emission inhibition is observed (Fig. 3(a)). In this regime, $\gamma_{0,I}$ is as high as 15 % of the total emission rate (30 % for emission in both $\pm z$ directions). The decreased type-I contribution at larger t_{slab} is due to a reduction of both its fiber-fraction $f_{0,I}$ and modal emission rate $\gamma_{0,I}$, as shown in Figs. 8(b) and 8(d), respectively. Along with its increased fiber fraction $f_{0,II}$, this results in the type-II supermode power approaching that of the type-I supermode, in spite of its significantly reduced $\gamma_{0,II}$.

In comparison, the low η_{PL} obtained for z-polarized dipoles (Fig. 5(c)) is a consequence of the small mode emission rates (Figs. 8(e) and 8(f)). In both hybrid-TM and hybrid-TE modes, the z-electric field supermode components are dwarfed by the dominant, x- or y-field components, resulting in small effective areas for z-directed dipole moments. We note that the relatively poor coupling of z-dipoles can prove polarization sensitivity which can, for example, be used to determine the in-plane polarization of an embedded semiconductor quantum dot.

As was the case for the x -dipole, η_{PL} oscillates as a function of z , with a period that is dominated by the beating of these two main supermodes. In addition, η_{PL} decreases as a function of z , due to the decay of the various supermodes. However, this decay is significantly slower than that found in the x -dipole case, as leaky modes play a far less prominent role in PL collection here. Over all slab thicknesses, $n_i^{-1} \gtrsim 1440$ for type-II supermodes, corresponding to $N_{\delta=0.9} \gtrsim 24$ free-space wavelengths for a 10 % amplitude decay. A coupling length shorter than $31 \mu\text{m}$ thus allows for collection efficiencies at levels close to those plotted in Figs. 5 (b) and 5(c). For the type-I supermode, $N_{\delta=0.9} \gtrsim 554$, so that a collection level at least as high as this supermode's individual contributions (Figs. 8(c) and 8(e)) may be achieved over coupling lengths of several hundreds of microns.

4. Discussion

The results of Section 3 indicate that laterally bound or quasi-bound hybrid supermodes play an essential role in luminescence collection in the single-emitter probing technique described in this work (and schematically summarized in Fig. 1). The overall PL collection efficiency depends on four interdependent parameters for each supermode: total (Γ) and modal (Γ_m) spontaneous radiation rates, fiber-mode fraction (f_m), and the supermode decay rate ($\alpha_{z,m}$). High fiber-mode fractions may be achieved by phase-matching the fiber and slab modes, however, a power shift toward the fiber can result in a reduced field concentration at the dipole position, and therefore smaller modal emission rates. A compromise between Γ_m and f_m determines the optimal collection efficiency. The decay rate $\alpha_{z,m}$ determines the length over which supermode collection is most efficient.

A first method to obtain a substantially enhanced collection efficiency is through a smaller diameter fiber. In Fig. 9(a), the maximum and minimum η_{PL} for an x -oriented dipole are plotted against slab thickness, for a 300 nm radius fiber (the same procedure which produced Fig. 5 was used, and the 500 nm radius results are re-plotted here). The maximum PL collection is in average 2.5 times that for a 500 nm fiber, while the minimum efficiencies are increased in average by one order of magnitude, and vary between 2 % and 4 %. The collection enhancement is due to the increased slab-like and leaky supermode PL contributions (Fig. 9(b)), which result from increased fiber fractions (Fig. 9(c)) that are enough to compensate for a small decrease in the modal spontaneous emission rates. In addition, leaky modes play a more important role than in the $R = 500 \text{ nm}$ case, especially for $t_{\text{slab}} \gtrsim 180 \text{ nm}$. Among the leaky supermodes with $\eta_{\text{PL},m}$ above 1 % of the slab-like supermode's, the one with the lowest individual contribution has $n_i^{-1} \lesssim 167$, or $N_{\delta=0.9} \gtrsim 3$ wavelengths for 10 % amplitude decay. As such, the maximum collection efficiencies in Fig. 9(b) will occur for coupling lengths that are within several microns. The slab-like supermode has $N_{\delta=0.9} \gtrsim 382$, so collection at least as high as its contribution in Fig. 9(b) is achievable over lengths shorter than $\approx 500 \mu\text{m}$.

Our calculations also show good prospects for probing InAs quantum dots in non-suspended slab configurations, where a $\text{Al}_{0.7}\text{Ga}_{0.3}\text{As}$ (refractive index ≈ 3.0 at $\lambda = 1.3 \mu\text{m}$) substrate is present underneath the GaAs host layer. For a slab thickness of 250 nm, we find, similarly to the suspended membrane case, a slab-like supermode, several slab-concentrated leaky supermodes, and a fiber-like supermode, which in total yield a maximum collection efficiency of ≈ 1.6 %. The reduced collection with respect to the GaAs membrane case is primarily due to a reduction in the supermode effective areas, as fields extend over longer lengths inside the substrate. In addition, the supermode decay lengths significantly change. The fiber-like supermode, which provides the largest contribution to PL collection, drops to 90 % of its original amplitude in approximately $2 \mu\text{m}$. Probing lengths of a few microns are thus required for highly efficient PL collection. The slab-like and first slab-concentrated leaky supermodes have $N_{\delta=0.9} \approx 254$ and $N_{\delta=0.9} \approx 24$, respectively. For coupling lengths as long as $\approx 31 \mu\text{m}$, the collection efficiency is

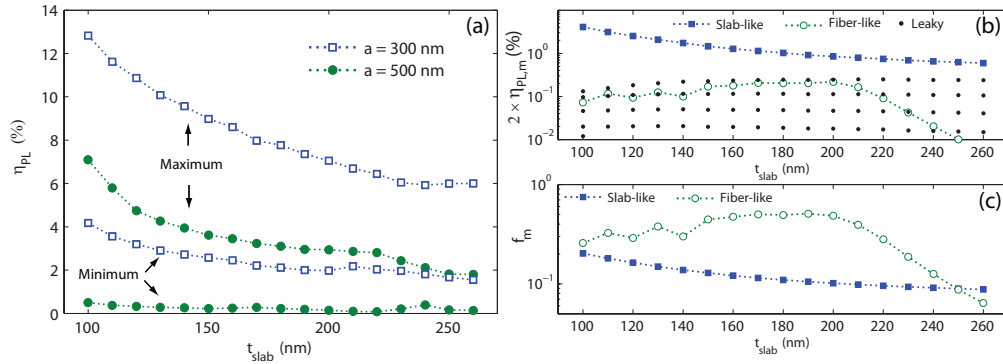


Fig. 9. (a) Total PL collection efficiencies (maximum and minimum values) for 300 nm and 500 nm radius fibers and an x -oriented dipole moment at $\lambda = 1.3 \mu\text{m}$. (b) PL collection contributions from the individual supermodes of the 300 nm radius fiber. The factor of 2 is to account for collection from both fiber ends. Filled squares/empty circles are for type I/II supermodes; black dots are for leaky modes. (c) Fiber fractions for type-I (filled squares) and type-II (empty circles) supermodes of the 300-nm radius fiber.

at least 0.13 %, the contribution of these two supermodes alone.

While the above cases and those studied in the rest of this paper largely involve a tradeoff between Γ_m and f_m , situations exist in which spontaneous emission enhancement and high η_{PL} can be reached through small effective area, high fiber-mode fraction supermodes. For example, this possibility arises for the hybrid-TM modes if a y -oriented dipole is placed between the fiber and slab. At $t_{slab} \approx 165$ nm, strong hybridization results in y -polarized supermodes with high confinement in the air gap, similar to the slot waveguide modes introduced in [26]. The spontaneous emission rate into this supermode alone reaches ≈ 1.7 times the homogeneous free-space rate, and the phase-matching between fiber and slab leads to a fiber-mode fraction close to 50 %. This indicates promising possibilities for fluorescence collection from dipoles located near the slab surface. Further investigation on single emitter spectroscopy applications utilizing this configuration is under way [27].

For the case of x -oriented dipoles, the collection efficiency may be effectively enhanced through stronger lateral confinement. In the hybrid-TE mode case of Section 3, PL collection efficiency is limited by the small fiber-mode fraction for the slab-like supermode and the even smaller fiber-mode fraction (and smaller spontaneous emission rates) for the slab-guided, leaky supermodes. To address these limitations, the slab may be converted into a suspended channel waveguide, which has been fabricated in a number of material systems, including recent experiments involving semiconductor quantum dots [28]. This structure provides guided supermodes with strong field confinement in the channel, so that the supermodes carry most of the emitted power, and may be designed to have high fiber-mode fractions, by phase-matching fiber and channel modes. As an example, for a channel thickness $t_{channel} = 256$ nm and width $W_{channel} = 250$ nm, two bound modes exist and carry ≈ 80 % of the total radiated power by an x -oriented dipole at the channel center. A total PL collection efficiency in excess of 70 % results. A detailed analysis of this system has been prepared [29].

Finally, we consider the potential for resonant fluorescence measurements within our fiber-based probing scheme. As mentioned previously, resonant spectroscopy offers many advantages in comparison to non-resonant PL measurements, most notably improved spectral resolution, avoidance of generation of decoherence-inducing excess carriers and well-defined state preparation [1, 2, 3, 4, 7, 12]. One of the main challenges in performing this type of spectroscopy is effectively isolating the residual or scattered resonant excitation beam from the resonance

fluorescence signal, as they occur at identical wavelengths (such separation is easily accomplished in non-resonant PL through a grating spectrometer or spectral filter). Recently, free-space optics collection of resonance fluorescence from a quantum dot inside a planar cavity was demonstrated [12]. In this work, separation of the fluorescence signal from the excitation beam was accomplished through an orthogonal excitation-collection scheme, where the sample was excited in-plane through a cleaved optical fiber, while the vertically emitted fluorescence was collected with a microscope objective.

Through the setup of Fig. 2(a), isolation of a resonant fluorescence signal can be achieved in a similar way. In a resonance fluorescence experiment, the pump signal (indicated in green in the figure) is tuned to the emitter transition. Illuminated by the resonant pump, the emitter radiates in both forward and backward directions of the fiber waveguide. The backward signal is routed to an external detector via a directional coupler, illustrated in Fig. 2(a), and is well-isolated from the pump signal (a fiber optic circulator could alternatively be used). Given the high fiber-collection efficiencies predicted in Fig. 5 (the collection in the backward channel will be $0.5\eta_{\text{PL}}$), this configuration may provide substantially superior signal-to-noise ratios in comparison to schemes that rely on free-space fluorescence collection. Alternately, we note that one might envision exciting the sample with a resonant free-space beam normal to the sample, while collecting the fluorescence through both the forward and backward channels of the fiber. This would create an orthogonal excitation-collection scheme similar to that of [12], with an overall efficiency given by η_{PL} as plotted in Fig. 5. Such a configuration may be preferable in situations where reflections in the fiber path between source and emitter can not be avoided.

5. Summary and Conclusions

A technique based on the use of an optical fiber taper waveguide for collecting emission from single emitters embedded in thin dielectric membranes was analyzed with numerical simulations. The probing configuration was modeled as a composite waveguide formed by a micron-scale silica fiber on top of a dielectric slab. Finite-difference time-domain simulations were used to estimate the efficiency with which emission from in-plane and vertically-oriented dipoles can be collected into the fundamental mode of the fiber. For in-plane dipoles, collection efficiencies superior to those achievable with a high numerical aperture objective are predicted, by as much as an order of magnitude. A maximum collection efficiency of $\approx 7\%$ may be obtained, with insignificant radiation suppression due to the slab. For vertically oriented dipoles, collection efficiency superior to free-space collection by at least an order of magnitude is predicted. A maximum collection above 35 % is obtained, albeit with strong slab-induced radiation suppression (Purcell factor of < 0.05). It is important to note that the presence of the fiber does not significantly affect the radiative rate of the slab-embedded dipole, so the suppression equally affects free-space collection.

Finite element simulations were used to understand the FDTD results through contributions from guided and leaky supermodes of the composite waveguide formed by the fiber and slab. Our analysis determined the essential role of laterally bound or quasi-bound hybrid supermodes in luminescence collection, as well as the relevant parameters for increased efficiency: total (Γ) and modal (Γ_m) spontaneous radiation rates, fiber-mode fraction (f_m), and the supermode decay rate ($\alpha_{z,m}$). In short, the ratio Γ_m/Γ (or, the supermode β -factor) and f_m must be maximized, while $\alpha_{z,m}$ must be minimized for higher collection levels. Potential methods to further increase the collection efficiency, based on supermode analysis, have been introduced. Furthermore, probing of single quantum dots in unprocessed (non-undercut) samples is predicted to yield collection levels on the same order as obtained with free-space collection. Finally, we have described how the probing method is amenable to both non-resonant photoluminescence and resonant fluorescence measurements.

In addition to efficient collection, optical fiber taper waveguides offer a number of benefits in the study of single solid-state emitters. These devices have standard single mode fiber input and output regions, and are therefore easily integrated with the technology of low-loss fiber optics. As discussed elsewhere [7], low-temperature measurement setups incorporating fiber taper waveguides and other fiber optic components have been used in cavity QED experiments in which precise knowledge of optical losses and power levels are a requirement. Furthermore, we note that as a movable probe, fiber taper waveguides have been used to interrogate two-dimensional arrays of devices on a chip [21]. The results of this article indicate that these advantageous features, previously demonstrated within the context of microcavity spectroscopy, can be utilized in direct single emitter spectroscopy.

Appendix A - Classical point dipole radiation in the presence of a waveguide

In this section, we demonstrate the validity of Eq. (10), which states that the ratio of the spontaneous emission rate in bulk to that in a waveguide is equal to the ratio of the total classical dipole radiated power in bulk to that in a waveguide. We consider a point dipole source $\mathbf{J}(\mathbf{r}, t) = -i\omega\mathbf{p}\delta(\mathbf{r})e^{-i\omega_0 t}$ radiating in the presence of an arbitrary, lossless dielectric waveguide extending along the z direction. The electromagnetic field may be expanded in terms of the bound and radiative modes of the waveguides as [13]:

$$\begin{aligned} \begin{Bmatrix} \mathbf{E} \\ \mathbf{H} \end{Bmatrix} &= \sum_j \left[a_j(z) e^{i\beta_j z} + a_{-j}(z) e^{-i\beta_j z} \right] \begin{Bmatrix} \mathbf{e}_j \\ \mathbf{h}_j \end{Bmatrix} + \\ &\sum_j \int d\beta \left[a_j(z, \beta) e^{i\beta z} + a_{-j}(z, \beta) e^{-i\beta z} \right] \begin{Bmatrix} \mathbf{e}_j(\beta) \\ \mathbf{h}_j(\beta) \end{Bmatrix} \end{aligned} \quad (\text{A-1})$$

with amplitude coefficients

$$a_{\pm j}(z) = \begin{cases} 0 & \text{for } z \geq 0 \\ i \frac{\omega_0 \mathbf{p} \cdot \mathbf{e}_j^*}{4N_j} & \text{for } z \leq 0 \end{cases} \quad \text{and} \quad a_{\pm j}(z, \beta) = \begin{cases} 0 & \text{for } z \geq 0 \\ i \frac{\omega_0 \mathbf{p} \cdot \mathbf{e}_j^*(\beta)}{4N_j(\beta)} & \text{for } z \leq 0 \end{cases}. \quad (\text{A-2})$$

The modes are such that the following orthogonality relations are valid:

$$\left| \iint_S (\mathbf{e}_j \times \mathbf{h}_k^*) \cdot \hat{\mathbf{z}} \right| = N_j \delta_{j,k}, \quad (\text{A-3})$$

$$\left| \iint_S [\mathbf{e}_j(\beta) \times \mathbf{h}_k^*(\beta')] \cdot \hat{\mathbf{z}} \right| = N_j(\beta) \delta(\beta - \beta') \delta_{j,k}. \quad (\text{A-4})$$

The total power flowing through the waveguide at a position $z > 0$ is obtained by integrating $1/2 (\mathbf{E} \times \mathbf{H}^*) \cdot \mathbf{z}$ over the cross-section:

$$\mathbf{S}_z = \frac{|\mathbf{p}|^2 \omega_0^2}{2} \sum_j \left\{ \frac{|\hat{\mathbf{p}} \cdot \mathbf{e}_j|^2}{N_j} + \int d\beta \frac{|\hat{\mathbf{p}} \cdot \mathbf{e}_j(\beta)|^2}{N_j(\beta)} \right\}_{\mathbf{r}=0} \quad (\text{A-5})$$

We next normalize the guided and radiative mode fields as in Eqs. (7) and (8). The guided mode propagation constants β_j may be expressed as [13]

$$\beta_j = \omega_0 \mu_0 \frac{\iint_S dS \epsilon(\mathbf{r}) (\mathbf{e}_j \times \mathbf{h}_j^*) \cdot \hat{\mathbf{z}}}{\iint_S dS \epsilon(\mathbf{r}) |\mathbf{e}_j|^2} = \iint_S dS \epsilon(\mathbf{r}) (\mathbf{e}_j \times \mathbf{h}_j^*) \cdot \hat{\mathbf{z}} \quad (\text{A-6})$$

Considering the waveguide material to be non-dispersive, the modal group velocity may be written as [13]

$$v_{g,j} = \left(\frac{d\beta_j}{d\omega_0} \right)^{-1} = c\beta_j \left(\frac{c}{\omega_0} \right) \frac{N_j}{\iint_S dS \epsilon(\mathbf{r}) (\mathbf{e}_j \times \mathbf{h}_j^*) \cdot \hat{\mathbf{z}}}. \quad (\text{A-7})$$

Using Eqs. (A-7) and (A-6) and Eq. (A-8), the power through the waveguide cross-section, normalized to the homogeneous dipole power, Eq. (3) becomes:

$$\mathbf{S}_z = \sum_j \left\{ \frac{6\pi c^3 \beta_j'}{n\omega_0^2} |\hat{\mathbf{p}} \cdot \mathbf{e}_j|^2 + \int d\beta \frac{6\pi c}{\mu_0 n \omega_0^2} \frac{|\hat{\mathbf{p}} \cdot \mathbf{e}_j(\beta)|^2}{N_j(\beta)} \right\}_{\mathbf{r}=\mathbf{0}}. \quad (\text{A-8})$$

The same expression is obtained by normalizing the spontaneous emission rate Γ in Eq. (B-10) by the spontaneous emission rate of a dipole in a homogeneous dielectric medium, given by:

$$\Gamma_{\text{Hom.}} = \frac{\omega_0^3 |\mathbf{d}_{eg}|^2 n}{3\pi \hbar \epsilon_0 c^3}. \quad (\text{A-9})$$

To verify Eq. (10), we used FDTD to simulate a point dipole radiating at $\lambda = 1.56 \mu\text{m}$ near an optical fiber of index $n = 1.45$ and radius $a = 500 \text{ nm}$, surrounded by air. The radiated power ratio $P_{\text{WG}}/P_{\text{Hom.}}$ is compared to the spontaneous emission rate ratio $\Gamma_{\text{WG}}/\Gamma_{\text{Hom.}}$, calculated with the semi-analytical expressions of [8]. Figures 10(a) and 10(b) show the two ratios for radially and longitudinally oriented dipoles at position r along the radial direction.

The relation between the classical guided fiber mode power P_g/P_{WG} and spontaneous emission rate $\Gamma_g/\Gamma_{\text{WG}}$ ratios was also verified. The steady-state fields recorded at one of the waveguide edges were used in the overlap integral of Eq. (2), together with the fundamental fiber mode fields, to yield P_g . Figure 10(c) compares the ratios for the radially-oriented dipole as a function of its position r in the radial direction.

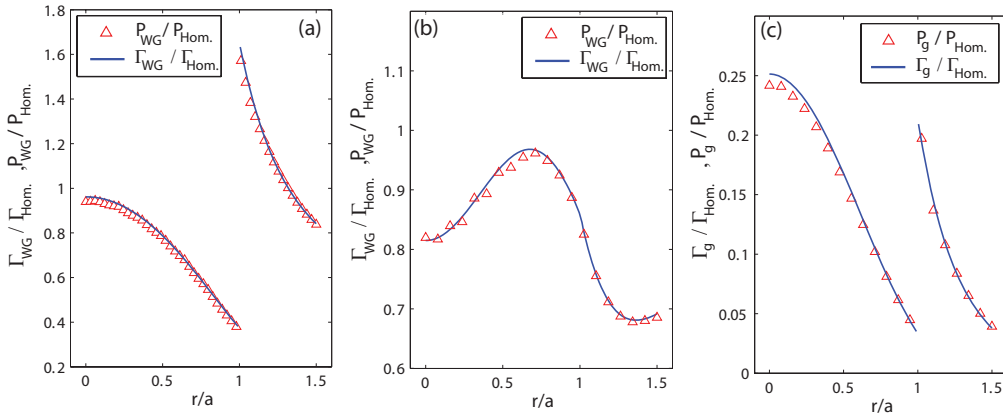


Fig. 10. (a) Emitted power and modal spontaneous emission rate at $\lambda = 1.56 \mu\text{m}$, normalized to the corresponding quantities in a homogeneous medium, for a (a) radially and (b) longitudinally oriented dipole at position r in the fiber described in the text. (c) Emitted guided mode power, P_g , and spontaneous emission rate, Γ_g , normalized to the total emitted power and emission rates, at $\lambda = 1.56 \mu\text{m}$ for a radially oriented dipole at position r in the fiber described in the text.

Appendix B - Heisenberg equations

To describe the spontaneous emission of a two-level emitter in the vicinity of a dielectric waveguide, we obtain the Heisenberg equations for the emitter interacting with a vacuum field reservoir that is described in terms of the guided and radiative waveguide modes propagating in the z -direction.

Through the quantization procedure of [30], the positive-frequency electric field operators are defined as $\mathbf{E}^{(+)} = \mathbf{E}_{\text{guided}}^{(+)} + \mathbf{E}_{\text{radiative}}^{(+)}$, where

$$\mathbf{E}_{\text{guided}}^{(+)} = i \sum_{f,m} \int_0^\infty d\omega \sqrt{\frac{\hbar \omega \beta'_\mu}{4\pi\epsilon_0}} a_\mu \mathbf{e}_\mu e^{-i(\omega t - f\beta_\mu z)} \quad (\text{B-1})$$

$$\mathbf{E}_{\text{radiative}}^{(+)} = i \sum_n \int_0^\infty d\omega \int d\beta \sqrt{\frac{\hbar \omega}{4\pi N_v}} a_v \mathbf{e}_v e^{-i(\omega t - \beta z)} \quad (\text{B-2})$$

Here, as in Section 3, $\mu = (f, m, \omega)$ labels a guided mode of order m traveling in the direction $f \cdot z$, $f = \pm 1$, with propagation constant β_μ , and inverse group velocity $\beta'_\mu = \frac{d\beta_\mu}{d\omega} = v_g^{-1}$. \mathbf{e}_μ is the mode field profile and a_μ is the corresponding photon annihilation operator. In (B-2), $v = (n, \beta, \omega)$ labels a radiative mode of order n and propagation constant β , with \mathbf{e}_v the corresponding field profile and a_v the photon annihilation operator. The β -integral limits are such that evanescent radiation modes are excluded (e.g., $|\beta| < \omega/c$ if the waveguide is embedded in air) [23]. Also, N_v is such that

$$\iint_S dS (\mathbf{e}_v \times \mathbf{h}_{v'}^*) \cdot \hat{\mathbf{z}} = N_v \delta(\beta - \beta'). \quad (\text{B-3})$$

The guided and radiative field profiles are normalized as in Section 3, such that $[a_\mu, a_{\mu'}] = \delta(\omega - \omega') \delta_{ff'} \delta_{mm'}$ and $[a_v, a_{v'}] = \delta(\omega - \omega') \delta(\beta - \beta') \delta_{nn'}$.

Next, consider a two-level atom (emitter) in the dipole approximation, interacting with a photon reservoir. The atom has a dipole moment \mathbf{d}_{eg} for the transition with energy $\hbar\omega_0$ between the ground $|g\rangle$ and excited $|e\rangle$ states. We define the atomic transition operators $\sigma_- = |g\rangle\langle e|$, $\sigma_+ = |e\rangle\langle g|$, $\sigma_z = |e\rangle\langle e| - |g\rangle\langle g|$, such that the atomic Hamiltonian is $H_A = \hbar\omega_0 \sigma_z/2$. The total Hamiltonian for the interacting atom and reservoir is

$$H = H_A + H_R + H_{I_R}. \quad (\text{B-4})$$

The interaction Hamiltonian for electric dipole coupling is given by $H_{I_R} = -\mathbf{d}_{eg} \cdot \mathbf{E}$, which, in the rotating-wave approximation, may be written as [8]:

$$H_{I_R} = i\hbar \left\{ \sum_{f,m} \int_0^\infty d\omega \left[G_\mu^* a_\mu^\dagger \sigma_- e^{i(\omega - \omega_0)t} - G_\mu \sigma_+ a_\mu e^{-i(\omega - \omega_0)t} \right] \right\} \\ + i\hbar \left\{ \sum_n \int_0^\infty d\omega \int d\beta \left[G_v^* a_v^\dagger \sigma_- e^{i(\omega - \omega_0)t} - G_v \sigma_+ a_v e^{-i(\omega - \omega_0)t} \right] \right\}, \quad (\text{B-5})$$

with

$$G_\mu = \sqrt{\frac{\omega \beta'_\mu}{4\pi\epsilon_0 \hbar}} (\mathbf{d}_{eg} \cdot \mathbf{e}_\mu) \quad \text{and} \quad G_v = \sqrt{\frac{\omega}{4\pi N_v \hbar}} (\mathbf{d}_{eg} \cdot \mathbf{e}_v). \quad (\text{B-6})$$

The formal solutions of the field operators are [31]:

$$a_{\mu,v} = a_{\mu,v}(t_0) + G_{\mu,v}^* \int_{t_0}^t dt' \sigma_- e^{i(\omega - \omega_0)t'}. \quad (\text{B-7})$$

Under the Markoff approximations $\sigma_-(t - \tau) \rightarrow \sigma_-(t)$ and $G_{\mu,v}(\omega) \approx G_{\mu,v}(\omega_0)$, the following Heisenberg equations for the atomic operators may be obtained:

$$\frac{d\tilde{\sigma}_-}{dt} = -i\omega_0\tilde{\sigma}_- - \frac{\Gamma}{2}\tilde{\sigma}_- + \sigma_z \left(\sum_{f,m} \sqrt{\Gamma_\mu} g_{\mu,\text{in}}(t) + \sum_n \int d\beta \sqrt{\Gamma_v} r_{v,\text{in}}(t) \right), \quad (\text{B-8})$$

$$\begin{aligned} \frac{d\sigma_z}{dt} = & -\Gamma(1 + \sigma_z) - 2\tilde{\sigma}_+ \left(\sum_{f,m} \sqrt{\Gamma_\mu} g_{\mu,\text{in}}(t) + \sum_n \sqrt{\Gamma_v} r_{v,\text{in}}(t) \right) \\ & - 2\tilde{\sigma}_- \left(\sum_{f,m} \sqrt{\Gamma_\mu}^* g_{\mu,\text{in}}^\dagger(t) + \sum_n \int d\beta \sqrt{\Gamma_v}^* r_{v,\text{in}}^\dagger(t) \right), \end{aligned} \quad (\text{B-9})$$

with $\sigma_- = \tilde{\sigma}_- e^{i\omega_0 t}$,

$$\Gamma = \left(\sum_{f,m} \Gamma_\mu + \sum_n \int d\beta \Gamma_v \right), \quad (\text{B-10})$$

$$\sqrt{\Gamma_\mu} = \sqrt{2\pi} G_\mu(\omega_0) \quad \text{and} \quad \sqrt{\Gamma_v} = \sqrt{2\pi} G_v(\omega_0). \quad (\text{B-11})$$

To arrive at these results, the following input field operators have been defined [30]:

$$\begin{Bmatrix} g_{\mu,\text{in}}(t) \\ r_{v,\text{in}}(t) \end{Bmatrix} = \frac{1}{\sqrt{2\pi}} \int_{-\infty}^{+\infty} d\omega \begin{Bmatrix} \tilde{a}_\mu(t_0) \\ \tilde{a}_v(t_0) \end{Bmatrix} e^{-i\omega(t-t_0)} \quad (\text{B-12})$$

Here, $a_{\mu,v}(t_0) = \tilde{a}_{\mu,v}(t_0) e^{i\omega_0 t_0}$.

Acknowledgement

This work has been supported in part by the NIST-CNST/UMD-NanoCenter Cooperative Agreement.